ADVANCED QUANTUM TECHNOLOGIES
www.advquantumtech.com

Classification of Single-Photon Emitters in Confocal Fluorescence Microscope Images by Deep Convolutional Neural Networks

Dongbeom Kim, Seoyoung Paik, Jeongeun Park, Seung-Jae Hwang, Shinobu Onoda, Takeshi Ohshima, Dong-Hee Kim, and Sang-Yun Lee**

In the rapidly evolving field of quantum information technology, the accurate and efficient classification of single-photon emitters is paramount. Traditional methods, which rely on conducting time-intensive Hanbury Brown-Twiss (HBT) experiments to acquire the 2nd-order correlation function of photon statistics, are not efficient. This study presents a pioneering solution that employs Deep Convolutional Neural Networks (CNNs) to classify single-photon emitters in confocal fluorescence microscope images, thereby bypassing the need for laborious HBT experiments. Focusing on the nitrogen-vacancy centers in diamond, the model is trained using fluorescence images of emitters that have been previously classified through HBT experiments. Applied to unclassified fluorescence images, the model achieves up to 98% accuracy in classification, substantially accelerating the identification process. This advancement not only makes the classification workflow more efficient but also promises wider applicability across various color centers and isolated atomic systems that necessitate imaging for isolation verification. This research signifies a substantial advancement in the application of quantum technologies, leveraging the power of deep learning to optimize the utilization of single-photon emitters.

1. Introduction

The study of solid-state single-photon emitters, such as color centers in solids, is pivotal in quantum information technology, especially for quantum communication. These emitters are essential for spin-photon conversion, a critical component in quantum computing networks.[1–4] Creating these color centers within solids can be achieved artificially through methods such as ion implantation,[5,6] electron injection,[7] and laser writing.[8,9] However, isolating these color centers remains a challenge.[2,3] Additionally, the large focal volume of conventional optical microscopy compared to the atomic-scale color centers makes distinguishing individual emitters difficult when multiple emitters are present.[10–12]

The conventional method to identify single-photon emitters involves analyzing emitted photons' physical properties using confocal fluorescence microscopy. To confirm an emitter's single photon emitting characteristic, researchers measure its second-order correlation function in photon emission statistics $g^{(2)}(\tau)$, through the HBT experiment, analyzing the arrival time intervals between photons τ and verifying antibunching $g^{(2)}(0) = 0$.[13,14] Real experiments often encounter challenges due to stray photons, and detector dark counts, making ideal antibunching hard to achieve.[13,15] Also, noise in real experiments require significant time to achieve a high signal-to-noise ratio (SNR) sufficient for the single emitter classification.[16,17] Alternatively, when evaluating well-characterized color centers, it becomes feasible to distinguish single emitters through the measurement of the maximum photon emission rate, commonly referred to as the saturated count rate. Nevertheless, this endeavor also entails iterative measurements while altering optical pumping rates.[13,16]

When numerous emitters exist within a sample, identifying each emitter as a single entity is a time-consuming task. For these reasons, recent research has explored using machine learning for more efficient analyzing method of the $g^{(2)}(\tau)$ data.[17,18] While this research improved time efficiency, it has not simplified the conventional process significantly, which still involves conducting HBT experiments. Thus, there is a need for methods that bypass HBT experiments for efficiency.

Ideal single photon emitters create a 3D image resembling a point spread function (PSF) when viewed through imaging systems like confocal microscopy.[19] Therefore, analyzing whether confocal microscopy images match the PSF may allow for the classification of single photon emitters. However, due to the focal

D. Kim, S. Paik, J. Park, S.-J. Hwang, D.-H. Kim, S.-Y. Lee
Department of Physics and Photon Science
Gwangju Institute of Science and Technology
123 Cheomdan-gwagiro, Gwangju 61005, Republic of Korea
E-mail: dongheekim@gist.ac.kr; sangyunlee@gist.ac.kr
S. Onoda, T. Ohshima
National Institutes for Quantum Science and Technology
Takasaki, Gunma 370–1292, Japan

DOI: 10.1002/qute.202400173

volume being significantly larger than that of single photon emitters, accurately identifying them is challenging especially when they are in close proximity. Furthermore, the judgment process heavily relies on subjective factors influenced by visual perception, leading to significant variability in results and analysis time.

In this study, we utilize CNN, a model of deep learning, to perform single emitter classification efficiently. CNNs excel at image classification[20] and have been used in a wide range of fields such as gravitational waves in astrophysics,[19] quark/gluor discrimination in particle physics,[20] disease diagnosis in medicine,[21] and determining the color of a single emitter.[22] For our study, we used nitrogen-vacancy (NV) centers, a long-studied and well-characterized diamond defect that has been prominent in the fields of quantum network[4,23,24] and quantum sensing,[25,26] to obtain image training data for single emitter classification. We established two deep learning models using individual images of NV centers that were determined to be single emitters or non-single emitters by analyzing $g^{(2)}(\tau)$ through HBT experiments. The first model was trained using the individual NV center images acquired by confocal microscopy and the values of the laser power used for each acquired images since the brightness of a single emitter and the power of a laser are correlated.[13] For the second model, the values of the laser power used for each acquired images were not used to train the CNN model. The second model was used to identify single emitters among the multiple spots in wide area images with the classification accuracy of 91% while the first model was used to classify single emitters for individually focused images and 98% accuracy was obtained. This marks the first attempt to identify single photon emitters using deep learning, bypassing the need for HBT experiments and significantly improving efficiency. This method is useful not only for the diamond NV centers, but also for the various color centers in solids such as silicon carbide[16,27–33] and 2D materials.[34,35] We also expect that this method could be applied to other physical systems that require imaging of isolated atomic or atom-like physical systems, such as phosphorous donors in silicon observed by scanning tunneling microscopy,[36] and single atoms on surface,[37] promising advancements in imaging isolated atomic systems.

2. Methods

2.1. NV Center in Diamond as a Model Single-Photon Emitter

In our study, the NV center in diamond serves as the model for single-photon emitter. It is a point defect comprising a nitrogen impurity and a carbon vacancy in the diamond lattice. This defect is notable for its photon emission probability, which is highly dependent on the electron spin state leading to the high-fidelity spin-photon conversion.[3] This characteristic facilitates the development of various quantum technologies, including quantum communication, sensing, and computing, by employing the ground state electron spin as a qubit.[2,3]

The NV center exists in two charge states: NV^0 and NV^-, with our research focusing on NV^-. The spectrum of photons emitted from NV^- displays a 200 nm wide phonon-side band centered around 700 nm at room temperature.[2] Since we only use the NV center as a single-photon source, we do not need to consider electron spin and spin-dependent photon emission. Thus, we model the NV center as a three-level system, encompassing the ground state, excited state, and metastable state, as depicted in **Figure 1a**.[15] This model illustrates that with increasing optical pumping rates, the probability of photon emission rises before reaching saturation.

2.2. Second-Order Correlation Function for Traditional Classification

Identifying single-photon sources involves measuring the second-order correlation via the HBT configuration.[38] The experimental method depicted in Figure 1b is used to record the photon detection events at two output ports of a beam splitter over time, deriving the second-order correlation function as below,[13]

$$g^{(2)}(\tau) = \frac{\langle n(t)\, n(t+\tau)\rangle}{\langle n(t)\rangle \langle n(t+\tau)\rangle} \quad (1)$$

where t is the time at which the photon is detected, τ is the time interval between two photon measurement events, and $n(t)$ is the number of photons measured at t. This equation considers the timing and interval between photon detections, highlighting that ideal single emitters exhibit anti-bunching, where simultaneous multi-photon detections are impossible, indicated by $g^{(2)}(0) = 0$. On the other hand, when N photons emitted simultaneously, $g^{(2)}(0) = 1 - 1/N$ is given, which becomes $g^{(2)}(0) = 0.5$ for $N = 2$. However, real-world conditions, including background noise from various sources and dark count of the detector, complicate achieving ideal anti-bunching. Consequently, when the measured $g^{(2)}(0)$ is <0.5, it is accepted as an experimental evidence for a single photon emission.[13,15] Figure 1c shows a typical $g^{(2)}(\tau)$ function for the diamond single NV center measured in the home-built experimental setup described later. It typically takes 5–10 min to achieve sufficient SNR making the identification of multiple emitters time-intensive. This situation is depicted in Figure 1e that will be explained in more detail later.

2.3. Point Spread Functions of Single Emitters

This study aims to train a neural network using optically acquired images of single emitters, focusing on the PSF. The PSF describes the distribution of light from a point source as captured by an optical microscopy system.[39] In an ideal setting, as shown in Figure 1d, the 2D PSF appears as an Airy function on the focal plane, extending three-dimensionally to depict light distribution depth. For confocal fluorescence microscopy, which is diffraction-limited, the PSF's boundary is where light intensity falls to $1/e$ of its peak, with its radius defined by the formula $r \approx 0.51\lambda/NA$ where λ is the light source's wavelength, and NA is the optical system's numerical aperture.[39] With our setup using a $\lambda = 532$ nm wavelength and an $NA = 0.95$ objective, the PSF radius is $r \approx 300$ nm as close to the experimental obtained PSF radius of ≈400 nm as in Figure 1d. Given the NV center's atomic size, its image aligns closely with an ideal PSF. When multiple

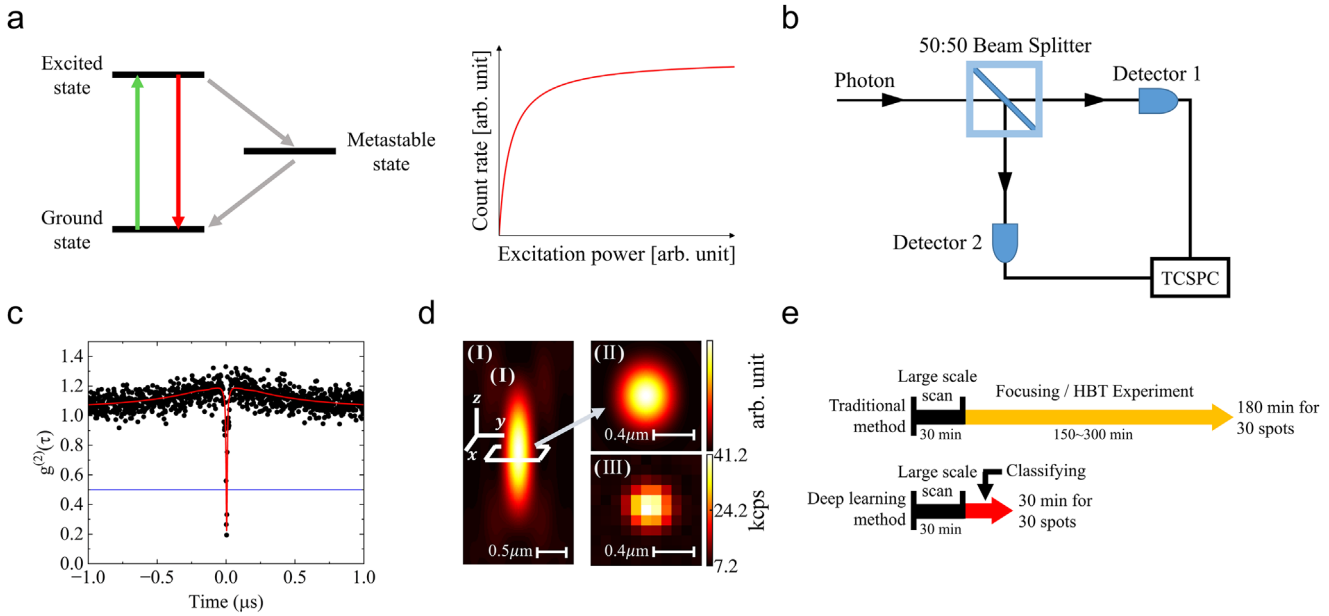

Figure 1. Diamond NV center as a model system. a) Energy levels of the NV centers and the typical photon emission rate as a function of optical excitation power of a three-level single-photon emitter. The photon emission rate saturates as the excitation power increases. b) Diagram illustrating the structure of the HBT experiment. TCSPC: time-correlated single photon counter. c) The measured second-order correlation function of a single NV center in diamond. d) Numerically calculated 3D Point Spread Function by using PSFLab (I), brightness distribution in the focal plane (II), and the actual image of single emitter in the focal plane (III). The image III is an example of the "focused emitter image". The brightness is indicated at the right axis as a unit of the detected photon counts per second (kcps). e) Timeline comparing the process of identification of a single emitter by using the traditional HBT experiments and the use of deep learning method. See text for detail.

point sources are closely spaced, the acquired image resembles the PSF of a single light source so that distinguishing them becomes challenging. This work demonstrates the effectiveness of deep learning in image-based single emitter classification, outperforming conventional approaches.

2.4. Sample Preparation and Experimental Methods

In this study, a diamond sample with an array of NV centers formed by ion implantation was used. The ion implantation was performed using a 10 MeV nitrogen micro ion beam.[40] Focusing the ion beam at desired positions with a dose of ≈500 ions per position created clusters involving many NV centers. We employed a home-built confocal fluorescence microscope to examine the single emitters. The sample was mounted on a piezo scanner capable of 1 nm precision movements in three dimensions. For excitation, we used a 532 nm laser directed through an NA = 0.95 objective, which also served to collect emitted photons. These photons were then filtered using a 685 nm long-pass filter before detection by single-photon detectors, employing an HBT setup for $g^{(2)}(\tau)$ measurements. **Figure** 2a depicts the schematic of the used confocal fluorescence microscope. Using this setup, an image for an array of NV centers was acquired, which is shown in Figure 2b.

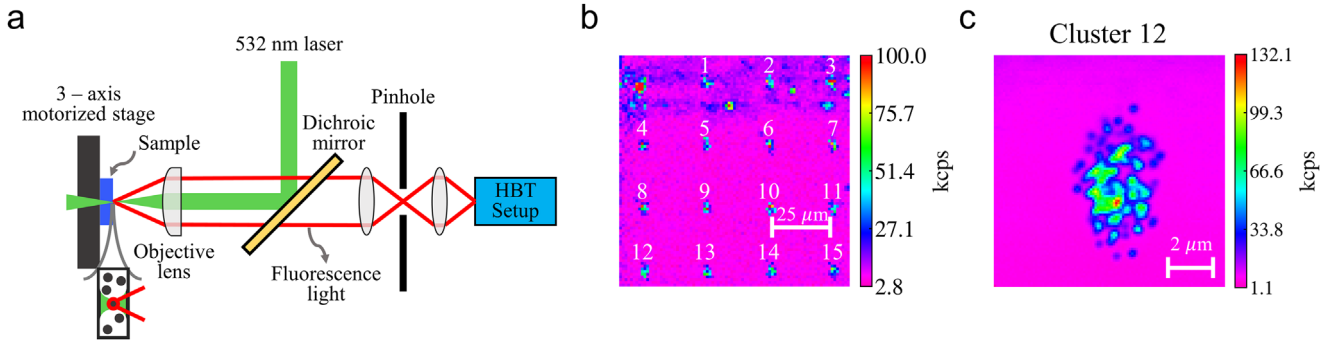

Figure 2. Experimental setup and confocal raster scan images. a) Home-built confocal fluorescence microscopy. The HBT setup is depicted in Figure 1b. b) NV center array generated by micro ion beam. A 100 μm × 100μm image reveals 15 bright clusters. The numbers are put to label each cluster. The several bright spots at the top left corner are due to the high dose implantation that was intentionally done to make a marker. Several bright spots not at the lattice points of the array are due to the misalignment of the ion beam. c) A 10 μm × 10μm "large-scan image" with a resolution of 0.1 μm from the cluster 12.

Table 1. Number of single and non-single data and laser input power for each cluster. The table displays the number of collected single and non-single data, as well as the input power, for each cluster.

Cluster #	1	2	3	4	5	6	7	8	9	10	11	12	13	14	15
Laser power (mW)	0.18	0.18	0.18	0.18	0.18	0.17	0.17	0.17	0.15	0.12	0.12	0.13	0.13	0.13	0.13
Single	10	3	8	12	16	13	13	14	12	11	14	17	15	11	15
Non-single	13	17	16	19	11	20	8	13	9	8	5	11	22	9	15

2.5. Data Collection and Preprocessing

We conducted a confocal raster scan across a 10 μm × 10μm region at 0.1 μm pixel spacing, centered on the brightest pixel in each cluster formed by ion implantation, across 15 clusters. These scans produced "large-scan images," exemplified in Figure 2c. Within these regions, we could identify many pixels showing the local maxima of the photon count rate, indicating potential emitters. Subsequently, 1 μm × 1μm "focused emitter images" were obtained under identical conditions for each potential emitter, with an example shown in Figure 1d. These images of 11 × 11 pixels were instrumental for training, as detailed later.

Each potential emitter underwent $g^{(2)}(\tau)$ function measurement, classifying it as a single emitter if $g^{(2)}(0)$ was below 0.5. In addition, we extracted the count rate of the background to remove its contribution. Nine emitters whose $g^{(2)}(0) < 0.5$ could not be determined within the margin of error were excluded. Also, laser power data for each emitter image were recorded for training purposes. This process yielded datasets for 380 emitters in total. In order to use both the brightness data and the laser power data as training data, both data were preprocessed to normalize the data to a normally distributed value.

The number of training data obtained from each cluster and the data of laser input power are shown in **Table 1**. Among the training data obtained by determining $g^{(2)}(0)$, there are 184 single emitters and 196 non-single emitters, demonstrating a balanced distribution for binary classification, mitigating bias towards either category. This balance extends to laser input power data, indicating no correlation between emitter type and laser power, further validating the dataset's suitability for unbiased classification.

The process explained above includes a conventional single emitter identification process using the $g^{(2)}(\tau)$ data; obtaining small size scanned image with high resolution to locate emitters and performing the HBT experiment to test whether $g^{(2)}(0) < 0.5$. As explained above, our motivation is to find a way to classify single emitters without performing this time-consuming process as described in Figure 1e. For this purpose, once the training was done, we tried to test the classification of single emitters only using the large-scan image (10 μm × 10μm size). Since the ion implantation results in the lateral distribution of the created NV centers, in a large area confocal raster scanned image with an arbitrary emitter in focus, not all the emitters are in the focal plane. To classify such emitters, we extracted 1 μm × 1μm "cropped emitter images" from bright spots in the large-scan images. To avoid judging background noise as a local maximum, we included only the cases in which the local maximum count rate is different from the minimum of the surrounding eight pixels by >4 kcps. These images were then used in deep learning models to identify single emitters, demonstrating a novel approach to emitter classification without extensive traditional methods.

2.6. Deep Learning Model Development

We developed a deep learning model that combines CNN for preprocessing of image data and a fully connected network for binary classification as sketched in **Figure 3**. Using a labeled dataset of experimental images prepared above, the model was trained to predict whether a given input image is of a single emitter. The model output $P(x)$ for a given input data x is often interpreted as a probability of x belonging to a target class in the sense of learning a binary distribution of labels with the cross entropy that we employed here for our model. For our dataset with balanced populations of the two classes, it is reasonable to set the prediction criterion to be $P_c = 0.5$ so that it can predict a given image data x to be a single emitter for $P(x) \geq P_c$ or a non-single emitter for $P(x) < P_c$. The detailed description of the model and the supervised learning procedures are provided in Supporting Information.

We considered two slightly different versions of the learning model. "Model I" additionally uses a laser power value that combines with the CNN-processed image data to make an input to the fully connected layer. On the other hand, "Model II" does not utilize the laser power information. We generated four candidates of the models for each of Model I and II and selected the one with the best test accuracy.

The purpose of introducing Model II is to deal with the issue of the large-scan images where the individual emitters are out of focus. Model I is designed to take advantage of the apparent correlation between the laser input power and the brightness of the focused emitters, achieving higher classification performance for small images where the laser power is likely to be proportional to the brightness. However, the large-scan images that are out of focus on the emitters unlikely exhibit such correlation, and Model II ignoring the laser power turned out to work better for the classification of the emitters in the cropped emitter images.

3. Results and Discussion

3.1. Classification Accuracy Using Focused Emitter Images

Now we present the results of the single emitter classification using Model I trained using the focused emitter images and the laser power data. **Figure 4** presents the results for the focused emitter image samples, comparing the exact manual classifications based on $g^{(2)}(0)$ with the automatic prediction results based

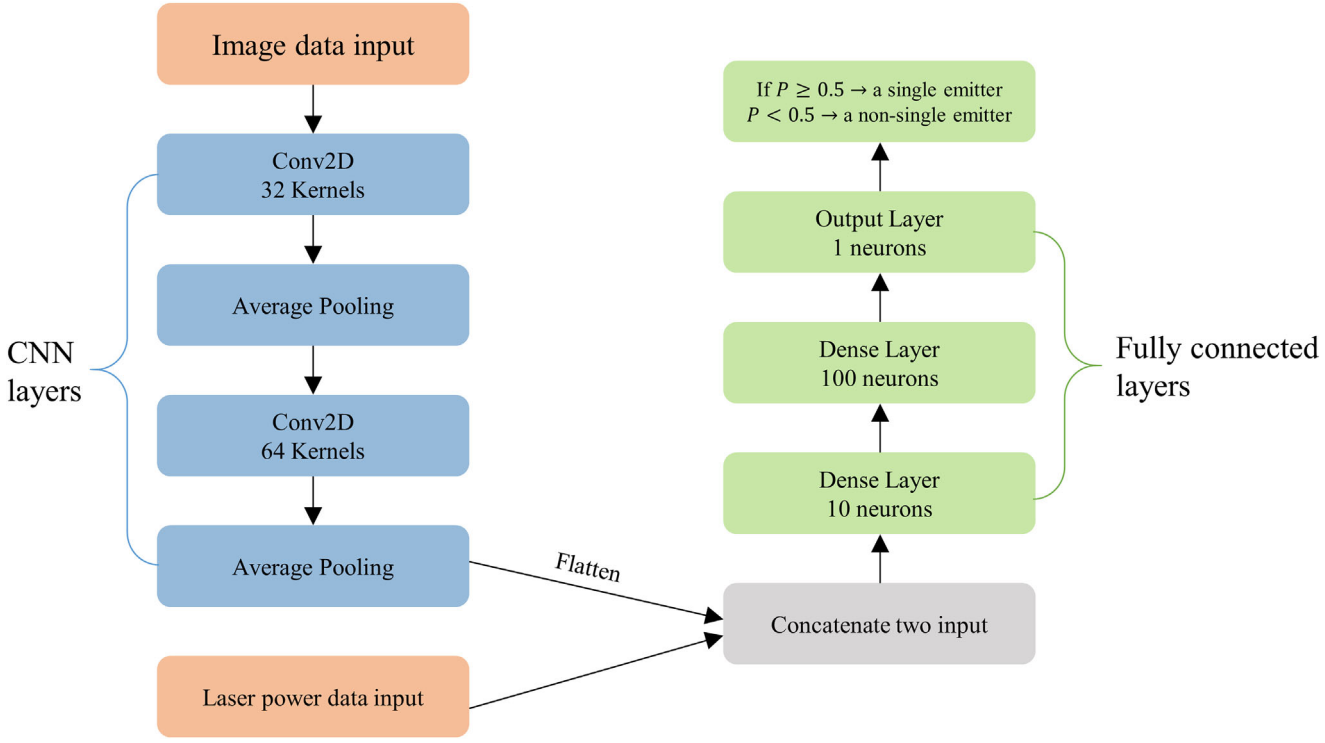

Figure 3. Schematic diagram of the neural network model. The brightness data of a given image in 11 × 11 pixels is processed through the CNN layers. The output from the CNN layers is optionally combined with the laser power data for Model I and then processed through the fully connected layers to make an output value *P* for binary classification.

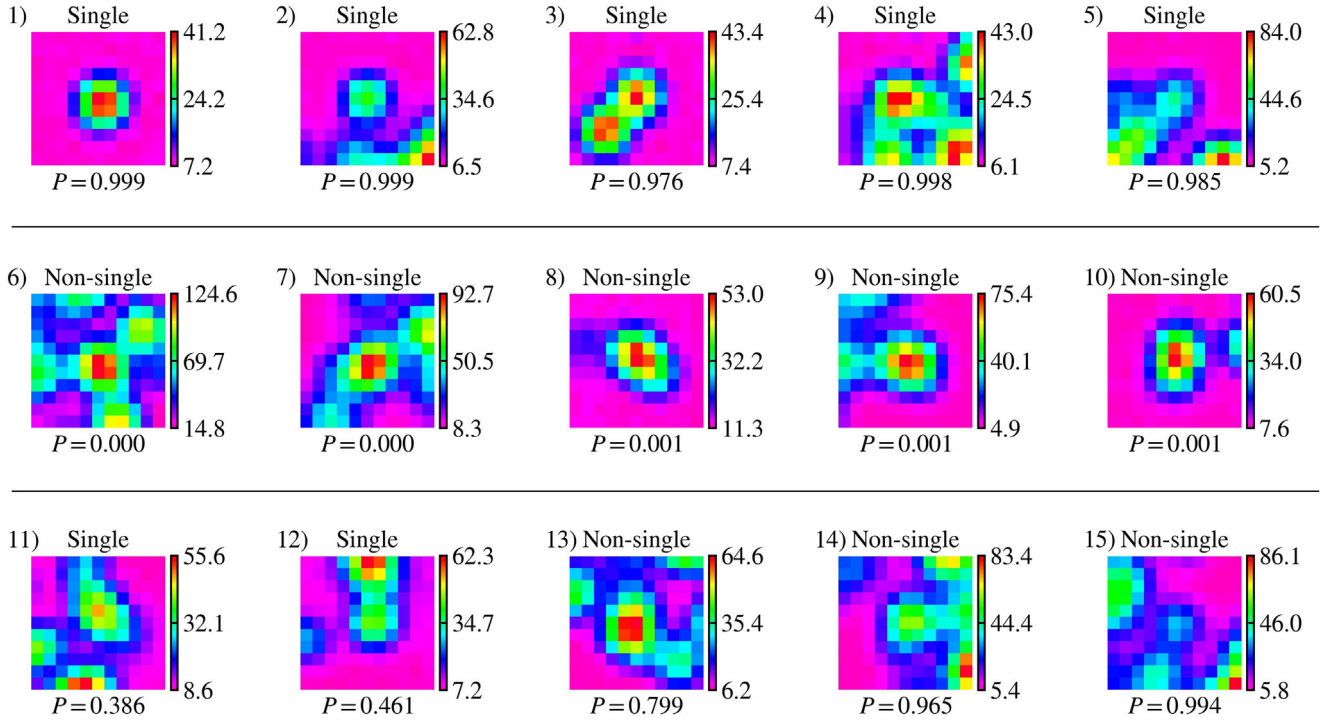

Figure 4. Examples of emitters images and predictions using Model I. The vertical color bars indicate the photon count rate in the unit of kcps. The manual identification of a "single" or "non-single" emitter based on $g^{(2)}(0)$ and the value of the model output *P* for the deep learning prediction are specified at the top and bottom of each image, respectively. The top and middle row present successful model predictions of single (top) and non-single (middle) emitters, and the bottom row presents rare failures of model predictions.

on the model output value P. The top row, from 1) to 5), shows the correct identification of the single emitters. While there are clear cases, such as 1) and 2), where the well-isolated single emitters are perfectly identified by $P \approx 1$, the predicting power of our model can be better demonstrated in the nontrivial cases where the emitters are not isolated. For such cases of 3), 4), and 5), where the emitters are close to each other, our model still correctly identifies a single emitter at the center with P higher than 0.98. Excellent performance can also be seen in the middle row from 6) to 10) as well, where the model prediction is successful for various types of non-single emitters, including the cases of non-isolated emitters and those similar to point sources. In particular, the non-single emitter of 8), which is correctly predicted by our model, is highly nontrivial because its brightness is similar to that of a single emitter.

Unsuccessful model predictions are found in only about two percent of the test data. The bottom row of Figure 4 shows such cases where the model prediction does not agree with the classification using $g^{(2)}(0)$. The images that lead to invalid model predictions have nontrivial features, such as in the single-emitter cases of 11) and 12) where the point source shape is hardly identified due to the surrounding emitters while the brightness is similar to that of a single emitter. However, it is generally challenging to decipher the mechanism of how a deep learning model selects information to process for classification because of its black box nature. In the following section, we will provide a brief discussion about the decision-making procedure of our CNN model and its black box nature more in detail.

The prediction accuracy of Model I is 0.979, which is the fraction of the cases giving correct predictions examined in the test dataset of the focused emitter images. The images used for the accuracy test were not included in the training and validation dataset of the supervised learning. We generated four candidates of the model that were trained with different selections of training and test data sets. While all results shown here are from the one with the best test accuracy that we finally selected for Model I, the accuracy difference between the model candidates are within just one percent (see Supporting Information for details). In addition, comparing with Model I, Model II exhibits a lower test accuracy of 0.905 for focused emitter images. The superior accuracy of Model I validates our idea of using the laser power as another input, which additionally utilizes the information that the brightness is related to the laser input power and their PSF.

A qualitative way of verifying the robustness of the model prediction is to see how sharply the model prediction distinguishes one class from the other. While our model prediction using the criterion $P_c = 0.5$ shows a good overall accuracy for the test data, an interesting question would be how well separated the value of P for a single-emitter data is from P of a non-single emitter data in the entire set of the images. For instance, one would not have much confidence if one had to make a binary classification based on the model output of 0.51 and 0.49. **Figure 5** addresses this question by showing the distribution of P over the test dataset and the dependence of the prediction accuracy on the values of P. The histogram of the model predictions presents sharp bimodal peaks near $P = 1$ and $P = 0$, demonstrating good distinguishability between the model predictions of different classes. The prediction accuracy measured for each histogram bin, namely the fraction of valid predictions among the cases having a value of P in the bin, indicates that the main loss of accuracy occurs for much less populated cases with P near 0.5. The high population of the predictions with $P = 1$ and $P = 0$ and their excellent accuracy indicates the excellent quality of our model training.

3.2. Classification Accuracy Using Large-Scan Images

This section evaluates Model II's performance on the cropped emitter images derived from large-scan images, where laser power is irrelevant because the image is out of focus and thus not considered in the model for large-scan images. The model was trained using the same labeled dataset of the focused emitter images. Among the four candidates generated, we selected the one with the best test accuracy of 0.905 for Model II. The accuracy difference of unselected candidates was about six percent. See Supporting Information for more details of the model training. Figure 5c,d demonstrates reasonably good performance of Model II in the test for the reliability of the prediction, where Model II and Model I exhibit qualitatively the same features, but Model II shows slightly reduced accuracy for the test data of focused images. Although, the genuine purpose of Model II is to go beyond the classification of the focused images.

We applied Model II to the dataset of 105 emitter images cropped from large-scan images. The cropped images belong to the selected clusters shown in **Figure 6** and are labeled as a single or non-single emitter using $g^{(2)}(0)$ data. Figure 6 compares the locations of single emitters manually identified using $g^{(2)}(0)$ with the single emitters identified from the automatic model predictions. The percentage of perfect matches is 89.5%, and this value is comparable to the accuracy seen above in the test with the focused images. This demonstrates the performance of our deep learning model as an automatic tool to identify single emitters within broader image scans, affirming its utility in efficiently pinpointing real single-photon sources by analyzing extensive scan data.

3.3. Black Box Nature of the Classification Process

In this section, we address the complexities surrounding how our CNN model makes classification decisions. This investigation is particularly prompted by the non-trivial cases highlighted in Figure 4 from Section 3.1. One of the tests involved comparing the final outputs of the CNN between successful and unsuccessful classifications. Although some differences were observed, we were unable to discern any systematic patterns that could reveal the decision-making process. This absence of interpretable patterns indicates that the processes within the CNN, particularly in the deeper layers, transform features into forms that are difficult to trace back to their original inputs. Given the complexity in deeper layers, our next investigation focused on the first layer, which would process the most direct features from the input images. We conducted numerical experiments using an artificially created ideal 2D PSF image to observe how initial inputs are transformed by this layer. We attempted to find a key image feature contributing to the model decision by testing a possible change in the model output against the deactivation of each filter in the first layer. However, these efforts also failed to yield significant insights into the classification mechanism, underscoring

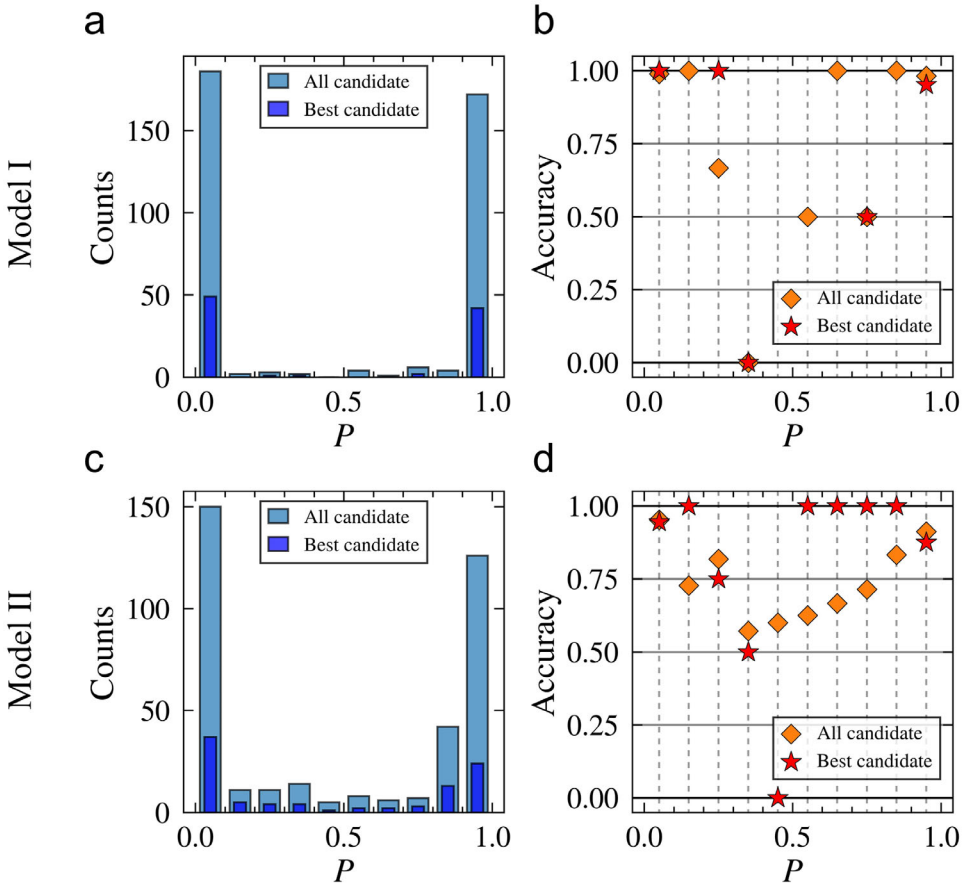

Figure 5. Accuracy and reliability of the single and non-single emitter classification. The left panels count the cases giving a model output P examined over the dataset of the focused emitter images using a) Model I and c) Model II. The bin size $\Delta P = 0.1$ is used to construct the histograms. In the right column, the accuracy of the prediction associated with a particular model output P of each bin is plotted for b) Model I and d) Model II. The bright blue bar in (a,c) and diamond symbols in (b,d) are the data from the test dataset of all candidate models while the dark blue bar in (a,c) and star symbols in (b,d) are from the test dataset of the best candidate.

the inherent challenges in interpreting CNNs. Details about the conducted tests can be found in the Supporting Information.

The black box nature may also influence the transferability of our CNN model, questioning whether a model trained on one system can be applied to another. The PSF image characteristics, including intensity and size, depend on experimental parameters like laser power and photon collection efficiency, which vary among different microscopes. Nonetheless, it is notable that our second model, trained without laser power information, successfully classified single emitters in large-scan images with 89.5% accuracy as discussed in the preceding sections. This success suggests that factors like laser power and photon collection efficiency might not be as crucial as the shape of the PSF for accurate classification.

Despite the successful application of the CNN model for single-emitter classification, further improvements in understanding the underlying mechanisms are needed for extension to broader applications. The "black box" nature of deep learning is a well-recognized challenge across various domains.[41,42] We plan to continue our efforts to unravel these complexities. A deeper understanding of the decision-making process could reveal key features necessary for accurate classification and enhance the model's robustness and adaptability across different setups.

4. Conclusion

Our research marks a significant breakthrough in classifying single-photon emitters by leveraging confocal fluorescence microscope imagery and laser input data, thus avoiding the time-intensive HBT experiments. Traditionally, the process of identifying and focusing on emitters has been time-consuming, but our method significantly reduces this with reaching 97.9% classification accuracy for focused images and 89.5% for broader scans. This efficiency, highlighted by a potential 90% time reduction, could revolutionize emitter studies in quantum technology. It suggests that further automation may eliminate the need for manual operation, dramatically enhancing both time and labor efficiency in this vital research area. Furthermore, our findings have profound implications for the development and deployment of quantum sensors, particularly those based on color centers in solids. The ability to accurately classify emitters within densely populated sensor arrays may enable the creation of more sensitive and specific sensors. In summary, our research not only

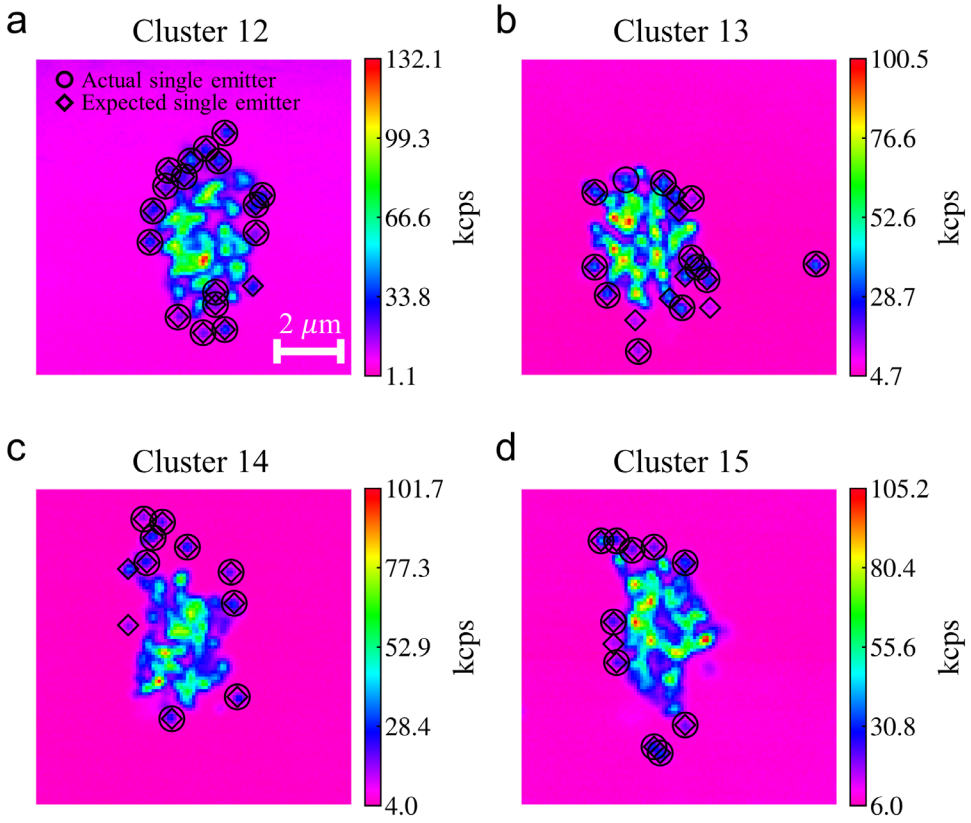

Figure 6. Identified single emitters and model predictions in large-scan images. In the images of the clusters 12–15, the circles indicate the locations of the single emitters that are manually determined using the $g^{(2)}(0)$ data, which is compared with the diamond symbols given to the prediction of the single emitters by Model II pre-trained earlier with focused images.

establishes a new benchmark in emitter classification but also lays the groundwork for significant advancements in quantum technology applications.

5. Experimental Section

The Sample Preparation: The ion implantation into a commercially available electronic grade diamond was performed using a microbeam system connected to a 3 MV Tandem accelerator at QST in Japan.[40] The $^{15}N^{3+}$ ions were accelerated to 10 MeV and focused into ≈2 μm in diameter. The microbeam was scanned at ≈500 ions per site to form a square grid of implantation sites spaced 25 μm apart in 200 × 200 μm^2. After implantation, the sample was treated with a hot mixed acid at elevated temperatures to remove impurities and replace the sample surface terminations with oxides. The temperature of the acid treatment was held at 200 °C for 30 min. After the acid treatment, ultrasonic treatment with acetone and Milli-Q water was performed for 10 min each. After hot mixed acid treatment, annealing was performed using an infrared heating furnace. With this system, the furnace chamber reached 1000 °C within 1 min and was held at 1000 °C for 2 h in vacuum. After annealing, the sample was again treated with hot mixed acid, acetone, and Milli-Q water.

Confocal Microscope and $g^{(2)}$ Function: A home-built confocal fluorescence microscope was used to detect photons from single emitters in diamond samples. The sample was mounted on a piezo scanner (PI Instrument P-562.3CD) that can be moved in three axes at 1 nm intervals. A 532 nm laser (CNI laser MGL-III-532) beam was reflected by a 600 nm long pass dichroic mirror, incident on an NA = 0.95 objective, and finally focused onto the sample. The light emitted by the single emitter was captured by the same objective and only photons that were filtered by the 600 nm long pass dichroic filter passed through the pinhole and reached the single photon detectors (Excelitas SPCM-NIR). An additional 685 nm long pass filter was installed in front of the photodetector for the further reduce of the background photons. An HBT configuration was formed using a 50:50 beam splitter behind the pinhole for $g^{(2)}(\tau)$ measurements as in Figures 1b and 2a.

Supporting Information

Supporting Information is available from the Wiley Online Library or from the author.

Acknowledgements

This research was supported by the National Research Foundation of Korea (NRF) funded by the Korean government (Ministry of Science and ICT(MSIT)) (No. 2021R1A2C2006904), the Institute of Information & communications Technology Planning & Evaluation (IITP) grant funded by the Korea government (MSIT) (No.2022-0-00198), MEXT Quantum Leap Flagship Program (MEXT Q-LEAP) Grant Number JPMXS0118067395, JST moonshot R&D Grant Number JPMJMS2062, and JSPS KAKENHI No. 21H04646.

Conflict of Interest

The authors declare no conflict of interest.

Data Availability Statement

The data that support the findings of this study are available from the corresponding author upon reasonable request.

Keywords

confocal fluorescence microscopy, deep learning, second-order correlation, single photon emitters

Received: April 15, 2024
Revised: July 8, 2024
Published online:

[1] S. L. N. Hermans, M. Pompili, H. K. C. Beukers, S. Baier, J. Borregaard, R. Hanson, *Nature* **2022**, *605*, 663.
[2] M. Atatüre, D. Englund, N. Vamivakas, S.-Y. Lee, J. Wrachtrup, *Nat. Rev. Mater.* **2018**, *3*, 38.
[3] D. D. Awschalom, R. Hanson, J. Wrachtrup, B. B. Zhou, *Nat. Photonics* **2018**, *12*, 516.
[4] M. Pompili, S. L. N. Hermans, S. Baier, H. K. C. Beukers, P. C. Humphreys, R. N. Schouten, R. F. L. Vermeulen, M. J. Tiggelman, L. dos Santos Martins, B. Dirkse, S. Wehner, R. Hanson, *Science* **2021**, *372*, 259.
[5] S. Pezzagna, D. Rogalla, H.-W. Becker, I. Jakobi, F. Dolde, B. Naydenov, J. Wrachtrup, F. Jelezko, C. Trautmann, J. Meijer, *Phys. Status Solidi* **2011**, *208*, 2017.
[6] I. Jakobi, S. A. Momenzadeh, F. F. de Oliveira, J. Michl, F. Ziem, M. Schreck, P. Neumann, A. Denisenko, J. Wrachtrup, *J. Phys. Conf. Ser.* **2016**, *752*, 012001.
[7] C. A. McLellan, B. A. Myers, S. Kraemer, K. Ohno, D. D. Awschalom, A. C. Bleszynski Jayich, *Nano Lett.* **2016**, *16*, 2450.
[8] Yu-C Chen, P S. Salter, S. Knauer, L. Weng, A C. Frangeskou, C J. Stephen, S N. Ishmael, P R. Dolan, S. Johnson, B L. Green, G W. Morley, M E. Newton, J G. Rarity, M J. Booth, J M. Smith, *Nat. Photonics* **2017**, *11*, 77.
[9] Y.-C. Chen, P. S. Salter, M. Niethammer, M. Widmann, F. Kaiser, R. Nagy, N. Morioka, C. Babin, J. Erlekampf, P. Berwian, M. J. Booth, J. Wrachtrup, *Nano Lett.* **2019**, *19*, 2377.
[10] Y. Silani, F. Hubert, V. M. Acosta, *ACS Photonics* **2019**, *6*, 2577.
[11] A. Gardill, I. Kemeny, Y. Li, M. Zahedian, M C. Cambria, X. Xu, V. Lordi, Á. Gali, J R. Maze, J T. Choy, S. Kolkowitz, *ACS Photonics* **2022**, *9*, 3848.
[12] S. Arroyo-Camejo, M. P. Adam, M. Besbes, J. P. Hugonin, V. Jacques, J. J. Greffet, J. F. Roch, S. W. Hell, F. Treussart, *ACS Nano* **2013**, *7*, 10912.
[13] S. C. Kitson, P. Jonsson, J. G. Rarity, P. R. Tapster, *Phys Rev A* **1998**, *58*, 620.
[14] C. Kurtsiefer, S. Mayer, P. Zarda, H. Weinfurter, *Phys. Rev. Lett.* **2000**, *85*, 290.
[15] I. Aharonovich, S. Castelletto, D. A. Simpson, C.-H. Su, A. D. Greentree, S. Prawer, *Rep. Progr. Phys.* **2011**, *74*, 76501.
[16] M. Widmann, M. Niethammer, T. Makino, T. Rendler, S. Lasse, T. Ohshima, J. Ul Hassan, N. Tien Son, S.-Y. Lee, J. Wrachtrup, *Appl. Phys. Lett.* **2018**, *112*, 231103.
[17] C. L. Cortes, S. Adhikari, X. Ma, S. K. Gray, *Appl Phys. Lett.* **2020**, *116*, 184003.
[18] Z. A. Kudyshev, S. I. Bogdanov, T. Isacsson, A. V. Kildishev, A. Boltasseva, V. M. Shalaev, *Adv. Quantum Technol.* **2020**, *3*, 2000067.
[19] R. Qiu, P. G. Krastev, K. Gill, E. Berger, *Phys. Lett. B* **2023**, *840*, 137850.
[20] P. T. Komiske, E. M. Metodiev, M. D. Schwartz, *J. High Energy Phys.* **2017**, *2017*, 110.
[21] A. Bin Tufail, Y. K. Ma, Q. N. Zhang, *J. Digit Imaging* **2020**, *33*, 1073.
[22] E. Hershko, L. E. Weiss, T. Michaeli, Y. Shechtman, *Opt. Expr.* **2019**, *27*, 6158.
[23] P. C. Humphreys, N. Kalb, J. P. J. Morits, R. N. Schouten, R. F. L. Vermeulen, D. J. Twitchen, M. Markham, R. Hanson, *Nature* **2018**, *558*, 268.
[24] C. T. Nguyen, D. D. Sukachev, M. K. Bhaskar, B. Machielse, D. S. Levonian, E. N. Knall, P. Stroganov, R. Riedinger, H. Park, M. Loncar, M. D. Lukin, *Phys Rev Lett* **2019**, *123*, 183602.
[25] C. L. Degen, F. Reinhard, P. Cappellaro, *Rev. Mod. Phys.* **2017**, *89*, 35002.
[26] J. M. Boss, K. S. Cujia, J. Zopes, C. L. Degen, *Science* **2017**, *356*, 837.
[27] Y.-C. Chen, P S. Salter, M. Niethammer, M. Widmann, F. Kaiser, R. Nagy, N. Morioka, C. Babin, J. Erlekampf, P. Berwian, M J. Booth, J. Wrachtrup, *Nano Lett.* **2019**, *19*, 2377.
[28] M. Widmann, S.-Y. Lee, T. Rendler, N. T. Son, H. Fedder, S. Paik, Li-P Yang, N. Zhao, S. Yang, I. Booker, A. Denisenko, M. Jamali, S. A Momenzadeh, I. Gerhardt, T. Ohshima, A. Gali, E. Janzén, J. Wrachtrup, *Nat. Mater.* **2015**, *14*, 164.
[29] C. Babin, R. Stöhr, N. Morioka, T. Linkewitz, T. Steidl, R. Wörnle, Di Liu, E. Hesselmeier, V. Vorobyov, A. Denisenko, M. Hentschel, C. Gobert, P. Berwian, G V. Astakhov, W. Knolle, S. Majety, P. Saha, M. Radulaski, N. T. Son, J. Ul-Hassan, F. Kaiser, J. Wrachtrup, *Nat. Mater.* **2021**, *21*, 67.
[30] N T. Son, C P. Anderson, A. Bourassa, K C. Miao, C. Babin, M. Widmann, M. Niethammer, J. Ul Hassan, N. Morioka, I G. Ivanov, F. Kaiser, J. Wrachtrup, D D. Awschalom, *Appl. Phys. Lett.* **2020**, *116*, 190501.
[31] D M. Lukin, C. Dory, M A. Guidry, Ki Y Yang, S. D. Mishra, R. Trivedi, M. Radulaski, S. Sun, D. Vercruysse, G Ho Ahn, J. Vuckovic, *Nat. Photonics* **2020**, *14*, 330.
[32] C. P. Anderson, E. O. Glen, C. Zeledon, A. Bourassa, Y. Jin, Y. Zhu, C. Vorwerk, A. L. Crook, H. Abe, J. Ul-Hassan, *ArXiv* **2021**, *8*, eabm5912.
[33] R. Nagy, M. Niethammer, M. Widmann, Yu-C Chen, P. Udvarhelyi, C. Bonato, J Ul Hassan, R. Karhu, I G. Ivanov, N. T. Son, J R. Maze, T. Ohshima, Ö O. Soykal, Á. Gali, S.-Y. Lee, F. Kaiser, J. Wrachtrup, *Nat. Commun.* **2019**, *10*, 1954.
[34] S. Gupta, W. Wu, S. Huang, B. I. Yakobson, *J. Phys. Chem. Lett.* **2023**, *14*, 3274.
[35] S. I. Azzam, K. Parto, G. Moody, *Appl. Phys. Lett.* **2021**, *118*, 240502.
[36] A. Morello, J. J. Pla, P. Bertet, D. N. Jamieson, *Adv. Quant. Technol.* **2020**, *3*, 2000005.
[37] A. J. Heinrich, J. A. Gupta, C. P. Lutz, D. M. Eigler, *Science* **2004**, *306*, 466.
[38] R. H. Brown, R. Q. Twiss, *Nature* **1956**, *177*, 27.
[39] R. W. Cole, T. Jinadasa, C. M. Brown, *Nature Protocols* **2011**, *6*, 1929.
[40] T. Yamamoto, T. Umeda, K. Watanabe, S. Onoda, M. L. Markham, D. J. Twitchen, B. Naydenov, L. P. McGuinness, T. Teraji, S. Koizumi, F. Dolde, H. Fedder, J. Honert, J. Wrachtrup, T. Ohshima, F. Jelezko, J. Isoya, *Phys. Rev. B Condens. Matter Mater. Phys.* **2013**, *88*, 075206.
[41] A. Barredo Arrieta, N. Díaz-Rodríguez, J. Del Ser, A. Bennetot, S. Tabik, A. Barbado, S. Garcia, S. Gil-Lopez, D. Molina, R. Benjamins, R. Chatila, F. Herrera, *Inform. Fusion* **2020**, *58*, 82.
[42] R. Guidotti, A. Monreale, S. Ruggieri, F. Turini, F. Giannotti, D. Pedreschi, *ACM Comput. Surv.* **2018**, *51*, 1.